AGU PUBLICATIONS

JGR

Journal of Geophysical Research: Oceans

RESEARCH ARTICLE

10.1002/2017JC012690

Key Points:
- Seismic evidence supports nonlinear internal wave pulse generation in the South China Sea by mechanism of geometric resonance
- We find heterogeneous diffusivity spanning two orders of magnitude around the Heng-Chun and Lan-Yu ridges similar to modeled shear zones
- Internal waves pulses exhibit similar turbulent signatures suggesting wave shape evolution during transit across the South China Sea

Correspondence to:
W. F. J. Fortin,
wfortin@ldeo.columbia.edu

Citation:
Fortin, W. F. J., W. S. Holbrook, and R. W. Schmitt (2017), Seismic estimates of turbulent diffusivity and evidence of nonlinear internal wave forcing by geometric resonance in the South China Sea, *J. Geophys. Res. Oceans*, *122*, 8063–8078, doi:10.1002/2017JC012690.

Received 9 JAN 2017
Accepted 10 AUG 2017
Accepted article online 21 AUG 2017
Published online 25 OCT 2017

Seismic estimates of turbulent diffusivity and evidence of nonlinear internal wave forcing by geometric resonance in the South China Sea

W. F. J. Fortin[1], W. S. Holbrook[2,3], and R. W. Schmitt[4]

[1]Lamont-Doherty Earth Observatory of Columbia University, Palisades, New York, USA, [2]Department of Geology and Geophysics, University of Wyoming, Laramie, Wyoming, USA, [3]Department of Geosciences, Virginia Tech, Blacksburg, Virginia, USA, [4]Department of Physical Oceanography, Woods Hole Oceanographic Institution, Woods Hole, Massachusetts, USA

Abstract The Luzon Passage generates some of the largest amplitude internal waves in the global ocean as the result of coupling between strong tides, strong stratification, and topography. These internal waves propagate into the South China Sea (SCS) and develop into soliton-like internal wave pulses that are observed by moored instruments and satellite backscatter data. Despite the observation of these waves, little is known of the mechanisms related to their evolution into nonlinear wave pulses. Using seismic data, we find evidence that the geometry of bathymetric conditions between the Heng-Chun and Lan-Yu ridges drive nonlinear internal wave pulse generation. We produce three seismic images and associated maps of turbulent diffusivity to investigate structure around the two ridges and into the SCS. We do not observe large amplitude soliton-like internal waves between the ridges, but do observe one outside the ridges, a finding in accord with the interpretation that wave pulses form due to geometrical resonance. Additionally, we find no evidence for lee wave activity above the ridges in either the seismic images or associated turbulence maps, suggesting an unlikelihood of hydraulic jump driven generation around the ridges. Our results show increased levels of turbulent diffusivity (1) in deep water below 1000 m, (2) associated with internal tide pulses, and (3) near the steep slopes of the Heng-Chun and Lan-Yu ridges as explored in this paper.

Plain Language Summary Localized pockets of highly turbulent waters likely play an important role in ocean mixing, but can be difficult to study by probing with traditional oceanographic methods as instruments cannot cover large swaths quickly in high resolution. Here we use seismic methods to estimate turbulent diffusivity in the South China Sea and show, across three 2D cross sections, patterns of elevated turbulence in the oceanic interior. Our findings show that internal wave packets generated by tides flowing over ocean ridges have similar turbulent "fingerprints." Additionally, we find no evidence that hydraulic jumps cause the generation of internal wave packets, but rather the local seafloor geometry is likely the driver of large internal wave generation in the South China Sea.

1. Introduction

1.1. Internal Waves in the South China Sea

Oceanic internal waves have been studied for decades to understand how energy is transported throughout the water column. Internal wave energy is quantified in terms of the observed canonical spectrum across scales of 100 km to 1 m [*Garrett and Munk*, 1975]. Recent work addresses tidal forcing, stratification, and the role of topography in the generation of regions with particularly high levels of internal wave energy, such as the Brazil Basin [*St. Laurent et al*., 2001] and the Hawaiian Ridge [*Rudnick et al*., 2003]. Regions of anomalously high internal wave energy input are important catalysts in driving ocean mixing as the input energy ultimately cascades from mesoscales to mixing scales [*Garrett*, 2003].

The Luzon Passage, which divides the western Pacific Ocean from the South China Sea, generates some of the most intense large-amplitude nonlinear internal waves in the world. In the Luzon Passage, internal waves can have displacement amplitudes of over 100 m and energy fluxes in excess of 100 kW/m [*Klymak et al*., 2006]. These internal waves generate disturbances at the sea surface large enough to be captured in satellite backscatter imagery as they propagate into the deep waters of the South China Sea [*Jackson*, 2007].

Both semidiurnal and diurnal tidal frequencies in wave pulses generated from the Luzon passage have been observed through remote sensing [*Zhao et al*., 2004] and moored instruments [*Ramp et al*., 2004]. Two major topographic features in the Luzon Passage, the Heng-Chun and Lan-Yu ridges, are responsible for the generation of the strong internal tides as seen in numerical models at local [*Jan et al*., 2008], regional [*Niwa and Hibiya*, 2001], and global scales [*Simmons et al*., 2004].

The role of the Heng-Chun and Lan-Yu ridges in internal wave pulse generation is still debated. Flow over seafloor ridges is capable of creating lee waves and hydraulic jumps, such as those seen in the Knight Inlet [*Farmer and Smith*, 1980] and the Strait of Gibralter [*Farmer and Armi*, 1988]. Hydraulic jump driven internal wave generation may account for the mixed semidiurnal and diurnal nature of the internal waves emitted into the South China Sea [*Ramp et al*., 2004] but would also necessitate the formation of lee waves [*Thorpe*, 2005]. However, direct evidence for lee waves or hydraulic jumps has not been reported in the Luzon Passage. An alternate explanation for sinusoidal, soliton-like internal wave generation at the ridges relies on the specific bathymetry and local tidal forcing. The geometry of the South China Sea amplifies the effect of tidal forces in 3-D models where resonance is boosted beyond idealized expectations of ridge height and separation by topographic blocking of barotropic flows [*Buijsman et al*., 2014]. Forcing due to geometric resonance would cause internal waves generated at the Lan-Yu Ridge to evolve into nonlinear wave pulses as the waves propagate over the Heng-Chun Ridge and through the SCS. This hypothesis may explain the absence of internal waves between the two ridges [*Jackson*, 2009].

Conventional oceanographic methods for observing internal wave generation and turbulent dissipation are challenging in the Luzon Passage due to the depth of the generating topography. While studies such as those in the Strait of Gibraltar [*Farmer and Armi*, 1988; *Wesson and Gregg*, 1994], the Bosphorus [*Gregg*, 2002], and the Knight Inlet [*Farmer and Smith*, 1980; *Klymak and Gregg*, 2004] image lee waves and associated levels of elevated dissipative turbulence, they are limited to the upper ~250 m of the water column due to attenuation of the high-frequency acoustic source. The geometry of the Luzon Passage requires deeper imaging in order to assess forcing parameters behind internal wave generation at the Heng-Chun and Lan-Yu ridges. The imaging and turbulence mapping methods of seismic oceanography are well suited to identifying lee waves and locating internal wave packets between and outside topographic ridges as key determinants in the understanding of internal wave energy in the South China Sea.

1.2. Seismic Oceanography

Seismic oceanography (SO) is a technique readily suitable for imaging internal wave forcing conditions in the Luzon Passage. By using a large amplitude, low-frequency (20–200 Hz) acoustic source, standard marine seismic equipment is capable of imaging the oceanic interior over the full ocean depth [*Holbrook et al*., 2003]. Reflections in the water column are the result of the interaction of the acoustic source wavelet with oceanic fine structure; using typical equipment, the method is sensitive to vertical temperature changes as small as 0.03°C [*Nandi et al*., 2004; *Sallarès et al*., 2009]. Processed SO data depicts a cross-sectional view of the oceanic interior where seismic reflections, typically shaded black/white for positive/negative seismic amplitudes, are essentially convolutions of the acoustic source wavelet with oceanic fine structure and represent approximate isopycnal surfaces laterally up to ~10 km [*Holbrook et al*., 2013].

Techniques in SO are able to estimate physical properties of the oceanic interior relevant to internal wave generation in the Luzon Passage. Internal wave energy has been estimated with seismic data by tracking seismic reflections and taking displacement spectra of the tracks [*Holbrook and Fer*, 2005; *Krahmann et al*., 2008]. Following techniques developed for estimating turbulence from isopycnal slope spectra [*Klymak and Moum*, 2007b], seismic reflector tracking can also estimate turbulent diffusivity over transects spanning many kilometers to full ocean depth accurately resolving lateral wavelengths down to ~25 m [*Holbrook et al*., 2013; *Sheen et al*., 2009] and vertical wavelengths of a quarter of the dominant frequency ~5 m. Seismic inversion techniques can also produce temperature and salinity profiles spanning tens to hundreds of kilometers [*Bornstein et al*., 2013; *Papenberg et al*., 2010; *Wood et al*., 2008]. The movement of water masses can even be recovered [*Huang et al*., 2012; *Klaeschen et al*., 2009].

Here we present seismic data from three transects crossing one or both ridges dividing the South China Sea from the Pacific Ocean to image the oceanic interior and provide estimates of turbulent diffusivity. These images and estimations of turbulence are then used to infer conditions surrounding the ridges. Our data provide evidence that geometric resonance is likely to be the dominant contributor to the formation of

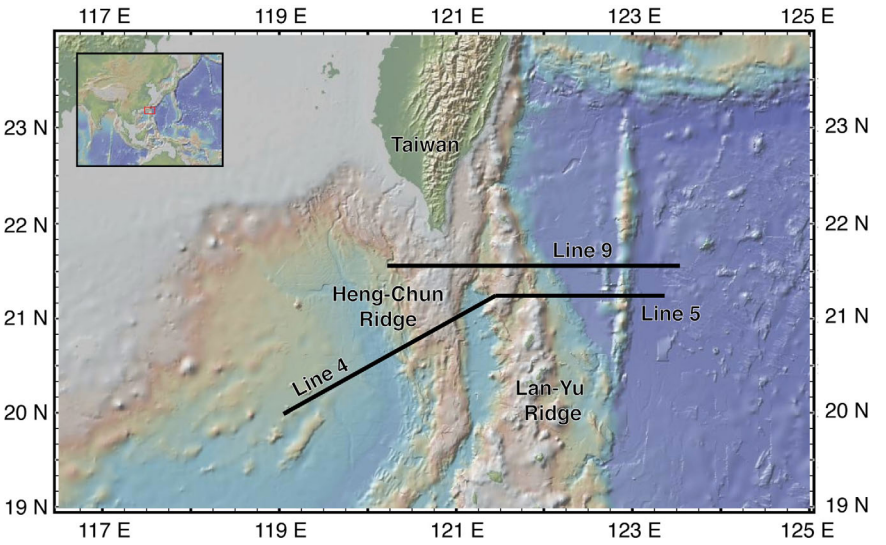

Figure 1. Map of seismic lines 4, 5, and 9 across the Luzon Passage.

nonlinear internal wave pulses observed in the South China Sea and highlights spatial heterogeneities in diffusivity around soliton-like internal waves and bathymetry.

2. Seismic Acquisition and Processing

Data used in this study were acquired aboard the *R/V Marcus Langseth* in June/July 2009 on leg 4 of the TAIGER project offshore Taiwan [*McIntosh et al*., 2014; *Wu et al*., 2014]. The acoustic signals were produced by a 36 element, 6600 cubic inch airgun array and recorded on a 480 channel, 6 km long streamer, yielding a horizontal sampling of 6.25 m at a sample rate of 2 ms. Data used in this study were collected with an acoustic source (shot) spacing of 50 m. Figure 1 shows the locations of the three transects presented in this study, lines 4, 5, and 9.

Data processing was completed in the manner required to reliably extract internal wave and turbulent energies from seismic data [*Fortin and Holbrook*, 2009; *Holbrook et al*., 2013]. Standard processing steps of geometry analysis, trace editing, filtering, CMP sorting, stacking, migration, and stretching to depth were applied [*Yilmaz*, 1987]. To fit the specific recommendations of *Holbrook et al*. [2013], data were filtered from 30 to 80 Hz and was checked for a signal to noise ratio of ~4. Sound speed analysis was executed using expendable bathythermograph instruments providing data quality suitable for spectral analysis [*Fortin and Holbrook*, 2009]. Specialized postprocessing was applied to remove harmonic noise cause by geometric move-up of the acoustic source and receiver stations [*Holbrook et al*., 2013]. Final seismic images, with subsurface geologic reflections muted, for line 4, 5, and 9 are shown in Figure 2.

3. Methods: Estimating Turbulent Diffusivity

Turbulent diffusivity from seismic data is calculated through slope spectral methods. Slope spectra are the horizontal gradient of vertical isopycnal displacements (ζ) and are calculated from temperature by $\zeta = z(T) - z_o(T)$, where $z_o(T)$ is the mean temperature profile. Vertical isopycnal displacements extend over four orders of magnitude in horizontal wave number [*Klymak and Moum*, 2007a,2007b] to horizontal wavelengths over 100m, a size well within seismic resolution. The turbulent portion of the slope spectrum, $\phi_{\zeta x}$, at seismic frequencies can be written as a function of turbulent dissipation (ε) in horizontal wave number (k_x) space:

$$\phi_{\zeta_x}^{Turb} = 4\pi \frac{\Gamma \varepsilon}{N_0^2} \left[C_T \varepsilon^{-\frac{1}{3}} (2\pi k_x)^{\frac{1}{3}} \right] \quad \text{(cpm)} \tag{1}$$

[*Holbrook et al*., 2013; *Klymak and Moum*, 2007b], where the empirical mixing efficiency, Γ, is 0.2 [*Osborn and Cox*, 1972], the constant C_T is set to 0.4 [*Sreenivasan*, 1996], and N_o is the mean buoyancy frequency.

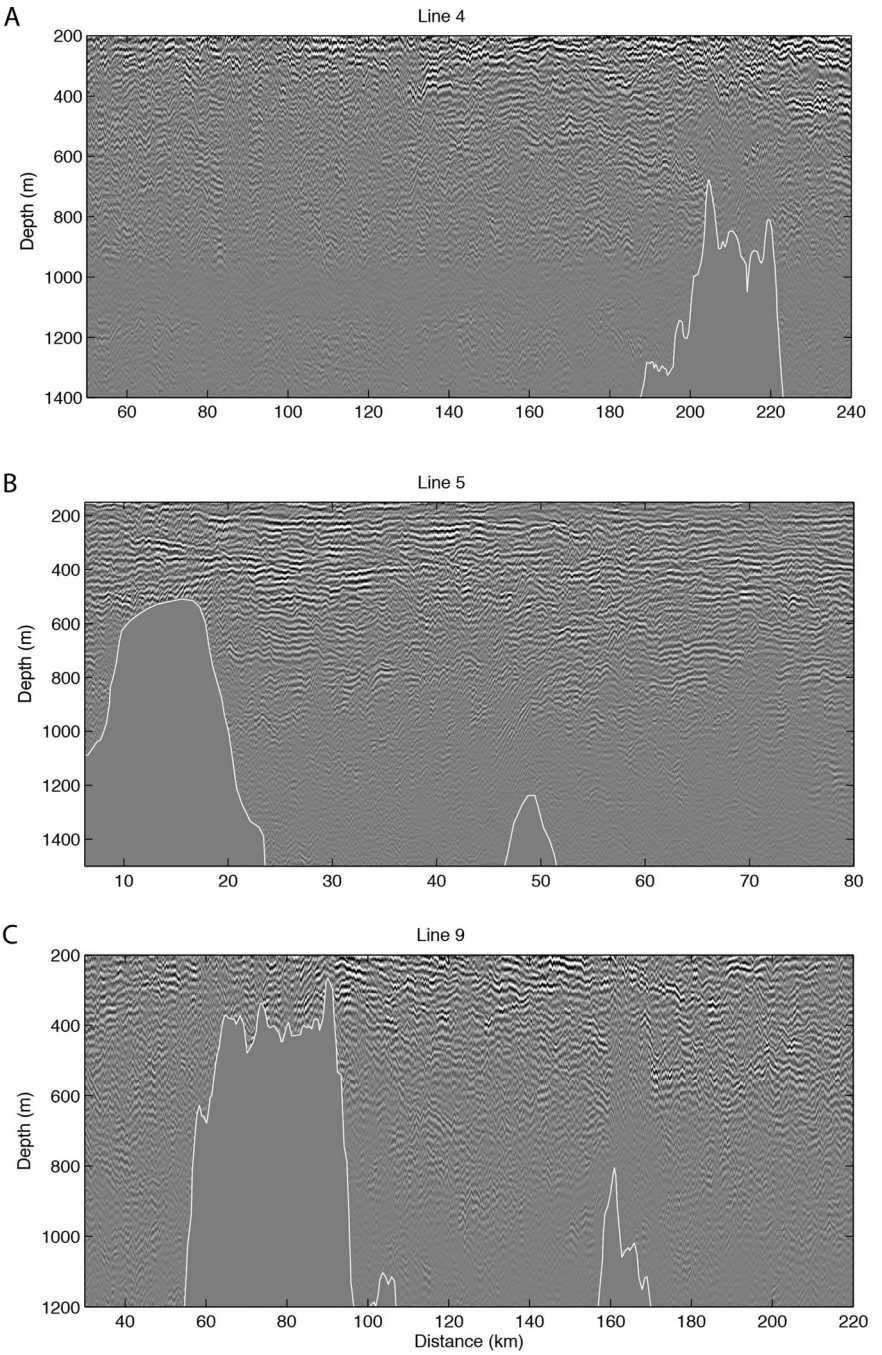

Figure 2. Seismic images of lines 4, 5, and 9.

Diffusivities (K_ρ) are calculated using $K_\rho = 0.2\varepsilon N^2$ [*Osborn*, 1980]. Equation (1) yields a characteristic slope of +1/3 for turbulence as a function of wave number in log-log space.

Two techniques of adapting slope spectral methods to seismic data are necessary to map diffusivity across entire sections following the technique of *Fortin et al.* [2016]: (a) seismic amplitude spectra taken along isobaths, also called data transforms and (b) displacement spectra from tracked seismic reflections. Data transforms relate seismic amplitude to horizontal wave number range by a Fourier transform [*Holbrook et al.*, 2013]. The data transform spans all wave numbers in a data volume, but produces spectra based on seismic amplitude, not levels of dissipation or diffusivity. Displacement spectra, in contrast, can accurately estimate internal wave and turbulent energy [*Eakin et al.*, 2011; *Holbrook and Fer*, 2005; *Holbrook et al.*, 2013;

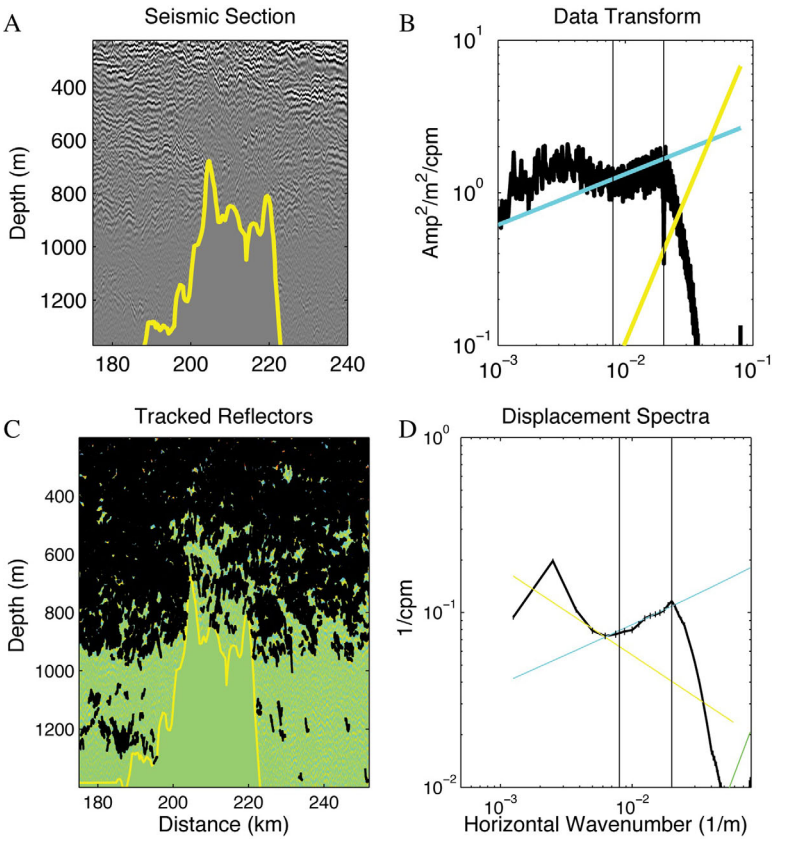

Figure 3. Data and spectra for line 4. (a) Seismic data and (b) associated data transform. The cyan line carries the characteristic +1/3 slope of turbulence, the yellow line the +2 slope of noise, and the vertical gray bars bound the turbulent subrange used in calculations. (c) The tracked seismic data in black used to make the displacement spectra in Figure 3d.

Krahmann et al., 2008; *Sheen et al.*, 2011, 2009] and are used to scale energy calculated from data transforms to absolute measures of diffusivity [*Fortin et al.*, 2016]. Since displacement spectra rely on large seismic amplitude returns they likely underestimate diffusivity values alone, but the data transform method utilizes all wave numbers thereby reintroducing weaker reflections caused by higher frequencies [*Fortin et al.*, 2016]. Reflector slope spectra are calculated as:

$$\phi_{Rx} = (2\pi k_x)^2 \phi_R \tag{2}$$

where ϕ_R is the displacement power spectrum [*Holbrook and Fer*, 2005]. ϕ_{Rx} is then scaled by buoyancy frequency, here assumed to be constant, and fit to $\phi_{\zeta x}$ of equation (1) by nonlinear least squares regression to provide an estimate if dissipation. Eddy diffusivity is estimated as $K_\rho = 0.2\varepsilon N^{-2}$ [*Osborn*, 1980].

The implementation of both spectral methods, the data transform and displacement spectra, is shown in Figures 3–5 corresponding to lines 4, 5, and 9. Figures 3a, 3b, 4a, 4b, and 5a, 5b show the data and calculated spectra via the data transform. Each data transform shows the seismic spectrum as a thick black line, the predicted +1/3 slope characteristic of turbulence in cyan, and the characteristic slope of noise in yellow. Noise carries a slope of +2 because the spectra are multiplied by k_x^2 for our implementation [*Klymak and Moum*, 2007b]. Vertical bars show the wave number range identified as the turbulent subrange. The tracks of seismic reflections and their slope spectra are shown in Figures 3c, 3d, 4c, 4d, and 5c, 5d. Estimates of turbulent diffusivity are achieved by fitting the characteristic +1/3 turbulence slope to the displacement spectra within the turbulent subrange [*Holbrook et al.*, 2013].

To produce the maps of turbulent diffusivity shown in Figures 6–8, data transforms are taken over normalized subsections of the seismic line. Here we use a subset window 400 m wide and 10 m deep to capture at least two horizontal wavelengths as calculated from the lower bound wave numbers in the turbulent subrange. The spectral energy is then integrated over the turbulent subrange and plotted to produce a map of

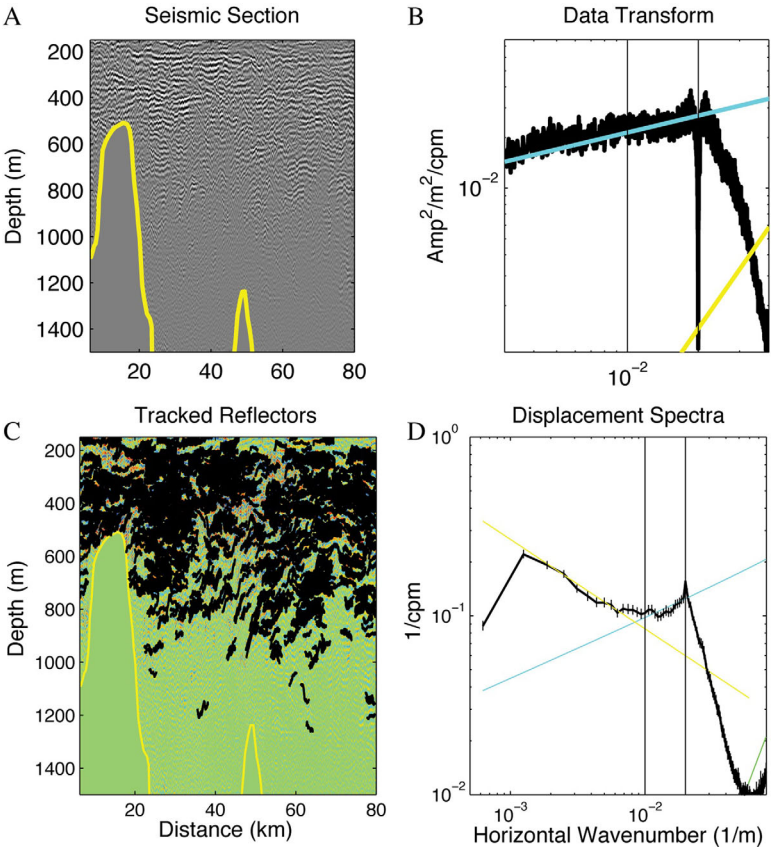

Figure 4. Data and spectra for line 5. (a) Seismic data and (b) associated data transform. (c) The tracked seismic data in black used to make the displacement spectra in Figure 4d.

relative turbulent energy across the section. The map is then scaled to absolute turbulent diffusivities calculated from displacement spectra of tracked seismic reflections in overlapping regional windows 3.2 km wide and 50 m deep to honor heterogeneity in turbulence across the image. The full details of turbulence mapping with seismic data can be found in *Fortin et al.* [2016].

4. Results

Here we present three seismic lines that each cross one or both ridges that run the length of the Luzon Passage. Each line was collected, and is presented here, in a west-to-east orientation. With signal to noise ratios of 4.6, 3.9, and 4.7, respectively, the data quality is sufficient for spectral analysis [*Holbrook et al.*, 2013]. Both data transforms and displacement spectra for all lines exhibit a distinct horizontal wave number subrange where spectral characteristics match predicted behavior for turbulence, i.e., a +1/3 slope (Figures 3–5).

4.1. Line 4

Seismic line 4 shows the most striking examples of heterogeneous structure of the three lines we present here; it is also most central to the Luzon passage and extends farthest into the South China Sea (Figures 1 and 2a). The entire water column contains thermohaline fine structure that produces seismic reflections, down to our processed depth of 1400 m. At 85 km, there is a vertically coherent, sinusoidal internal wave packet of amplitude of ~50 m moving at 1.2 m/s along the transect (see Figure 9a) [*Von Lanken*, 2012]. The speed of the wave packet was calculated by repeatedly imaging the wave shape using partial stacks of the seismic data and the speed is in agreement with a dynamic model [*Von Lanken*, 2012]. At the peak of the Heng-Chun Ridge at ~700 m, strong, continuous seismic reflections to the west of the ridge terminate at the seafloor high around 202 km. Above the ridge, seismic reflections are more interrupted and reflections strength diminishes. East of the ridge, past ~225 km, the strong, coherent seismic reflections resume. We

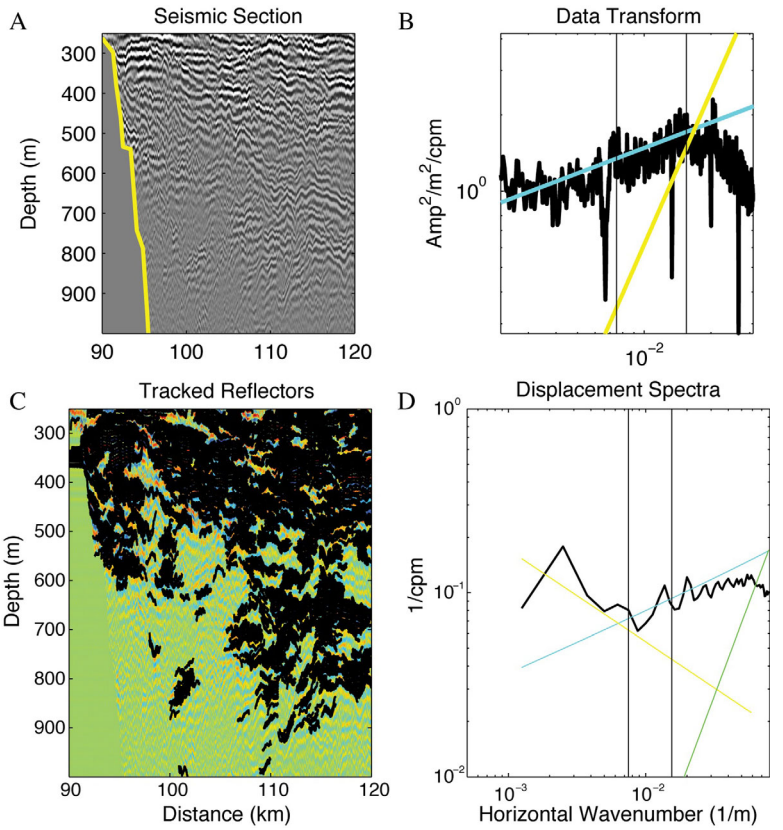

Figure 5. Data and spectra for line 9. (a) Seismic data and (b) associated data transform. (c) The tracked seismic data in black used to make the displacement spectra in Figure 5d.

also observe strong reflections bounding more seismically transparent layers, typically less than 100 m thick. These lenses are found most commonly near the seafloor ridge here, as well as in seismic transect 9.

Spectral characteristics of line 4 match predicted slopes for both internal waves and turbulence (Figures 3b and 3d). The wave number range where the data transform and displacement spectra of tracked reflections show the characteristic slope of turbulence is 0.008–0.02 cpm. Displacement spectra yield an average diffusivity of 1.1×10^{-4} m^2/s across the entire transect. Noise is not observed due to the diminished spectral

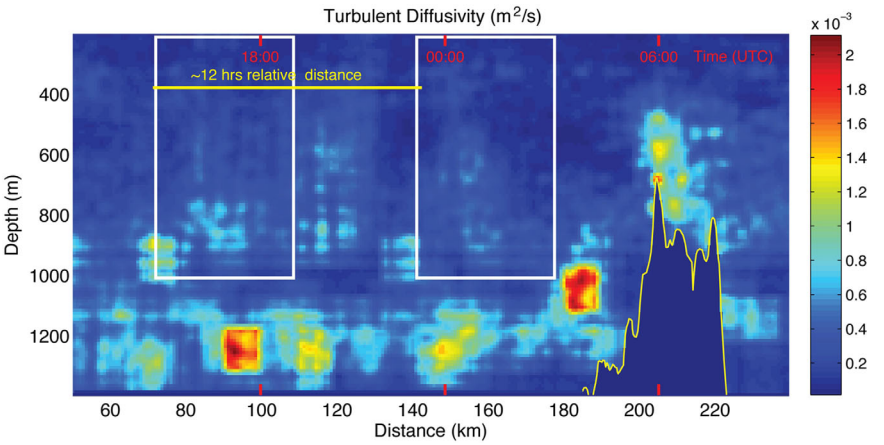

Figure 6. Turbulence map of line 4. Red ticks show the ship position at times (UTC) labeled in red. White boxes bound regions used in zoom Figure 11. Yellow bar shows the distance the ship travels in one 12 h semidiurnal period when scaled for relative motion to internal waves at speed 1.2 m/s.

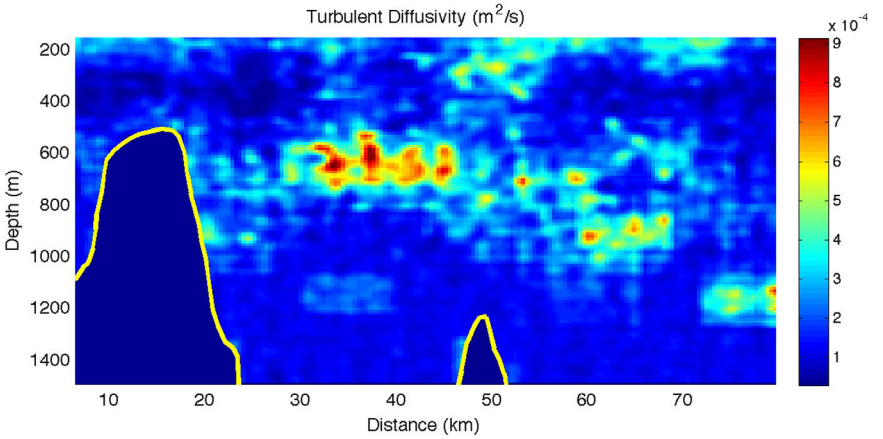

Figure 7. Turbulence map of line 5. Elevated diffusivity in midwater likely bounding water movement over the Lan-Yu ridge.

energy observed above the upper turbulent wave number limit, 0.02 cpm, due to the 30–80 Hz band-pass filter [*Holbrook et al*., 2013].

Estimated turbulent diffusivity across the lines is highly heterogeneous and strongest in deep water (Figure 6). The strongest turbulence is seen in "hot spots" at depth, and diffusivity levels below ~1000 m are consistently higher than those in more shallow water, a result also seen in current and hydrographic data. For example, *Tian et al*. [2009] show the importance of mixing in the South China Sea on the overall Pacific circulation and find that diffusivities below 1000 m occur due to a decrease in dissipation rate rather than an increase in buoyancy frequency. The findings of *Tian et al*. [2009] outline a qualitative relationship between the basins of the Luzon Passage, but call for further observation. Our seismic observations find mixing hot spots, likely expressed as turbulent rods in three dimensions, that churn the deep waters in the South China Sea and Luzon Strait. In situ measurements show more homogeneously elevated diffusivities while seismic methods are mottled. It is likely that strain caused by tidal forcing creates stronger density and sound speed fine structure gradients that produce seismic reflections while the in situ measurements are capable of recording diffusivity even where seawater property gradients are too low for seismic methods. Further testing using both in situ and seismic methods are required to determine if such a mechanism is at play in the deep water of the South China Sea.

The seismic image is disrupted between depths of 1000 and 1150 m as the result of seismic amplitude gain control in data processing resulting in a band of low reflectivity visible in the seismic data and artificial horizontal banding in the diffusivity map. Though weak in amplitude at the scale of Figure 6, there is vertical

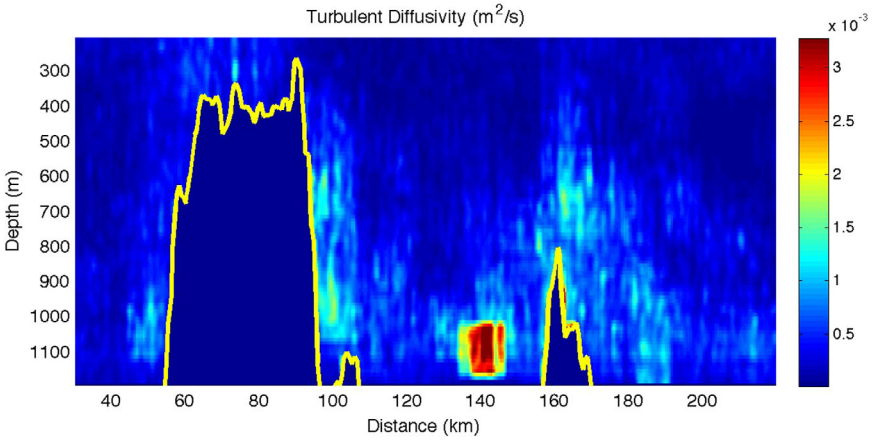

Figure 8. Turbulence map of line 9. Elevated diffusivity is primarily in deep water and above the eastern Lan-Yu ridge.

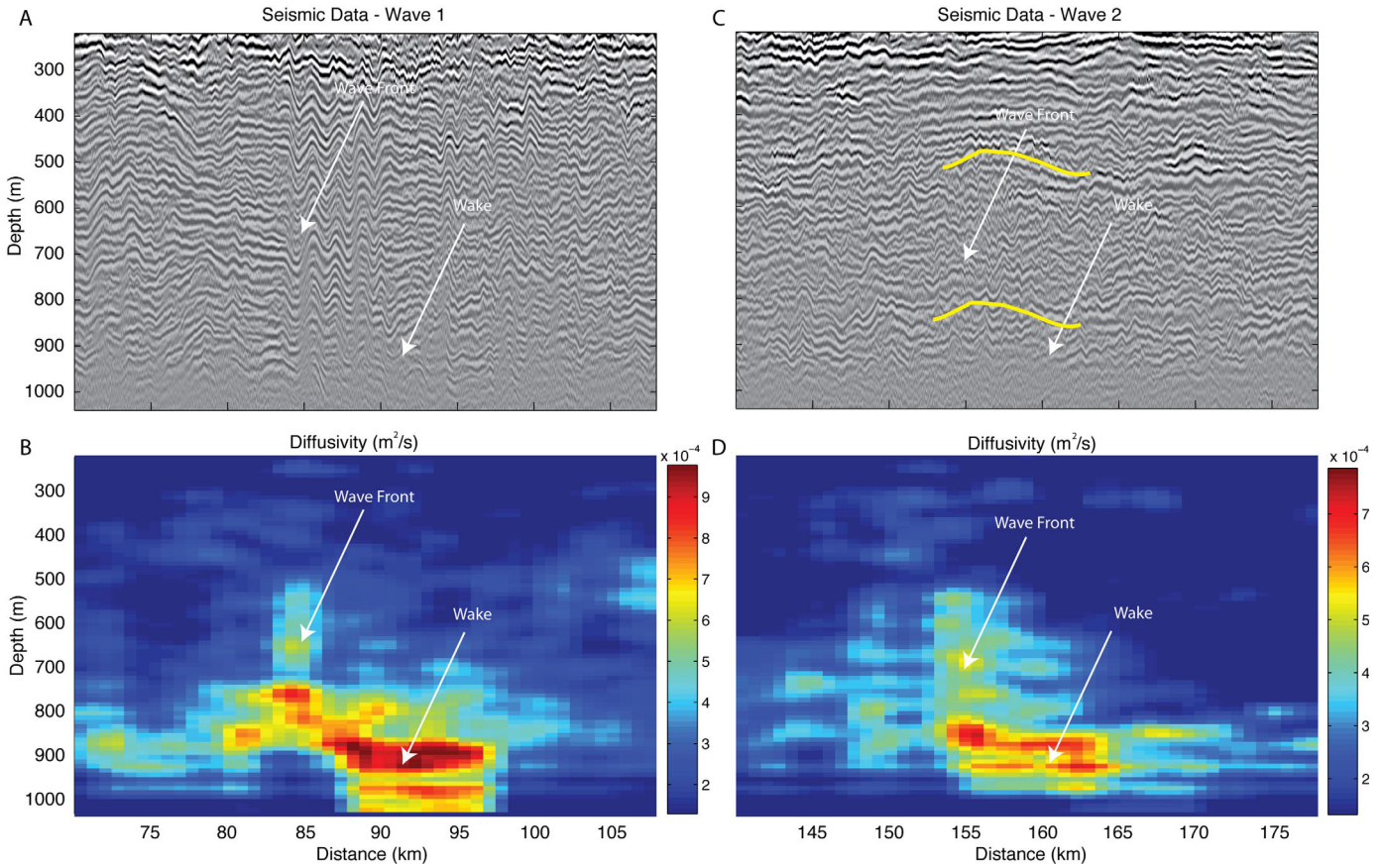

Figure 9. Comparison of two internal wave packets. (a) Seismic image of a sinusoidal internal wave. (b) Diffusivity created by a moving internal wave. Note the elevated levels at the leading edge and wake below/behind the vertically coherent wave packet. (c) Seismic image of a lower horizontal wave number displacement to seismic reflections, traced in yellow. (d) Diffusivity associated with seismic image in Figure 9c shows very similar pattern to the clear, sinusoidal internal wave packet in Figure 9a.

banding west of the ridge down to depth of ~1000 m caused by internal waves traveling through the water column.

Internal waves propagating through the water column exhibit a characteristic spatial turbulence signature. The highly sinusoidal internal wave packet and its associated turbulence map is highlighted in Figures 9a and 9b and is clearly seen between 85 and 90 km as a vertically coherent waveform from 300 and 900 m depth. At the leading edge, levels of turbulent diffusivity are elevated 3–5 times that of surrounding waters ahead and behind the wave packet. This result is likely the result of changing fine structure as the internal wave pulse begins to alter the existing oceanic layers. Diffusivity is significantly increased in a "wake" below and behind the wave packet to levels 15 times greater than surrounding waters. The dominance of turbulence below the wave pulse, instead of above, is likely the result of deeper waters being less strongly stratified as evidenced by reduced seismic amplitudes. Using the ship velocity, 2.5 m/s east along line, and the velocity of the wave packet along our seismic line, 1.2 m/s west along line, we calculate a relative distance the ship travels in a semidiurnal 12 h period as $D = c_s T(c_s/(c_s + c_w))$, where c_s is the ship speed, T is the semidiurnal period, and c_w is the wave speed, here ~73 km. Figures 9c and 9d show a window of data and its associated turbulence map, at the same scale as Figures 9a and 9b, one 12 h semidiurnal period after the wave packet at 85 km. While there is no clear sinusoidal wave packet similar to that observed at 85 km, there is a coherent long-wavelength disruption to the seismic reflections present at a similar lateral and vertical extent, a disruption of ~50 m amplitude and ~6 km length, traced in yellow (Figure 9c). The turbulence map shows a remarkable similarity to that of the wave packet at 85 km in shape, but is slightly lower in diffusivity values.

Increased diffusivity is also seen above the Heng-Chun ridge at magnitudes near those of the deep water. Figure 10 highlights the turbulence above the ridge top. In more seismically transparent zones, where

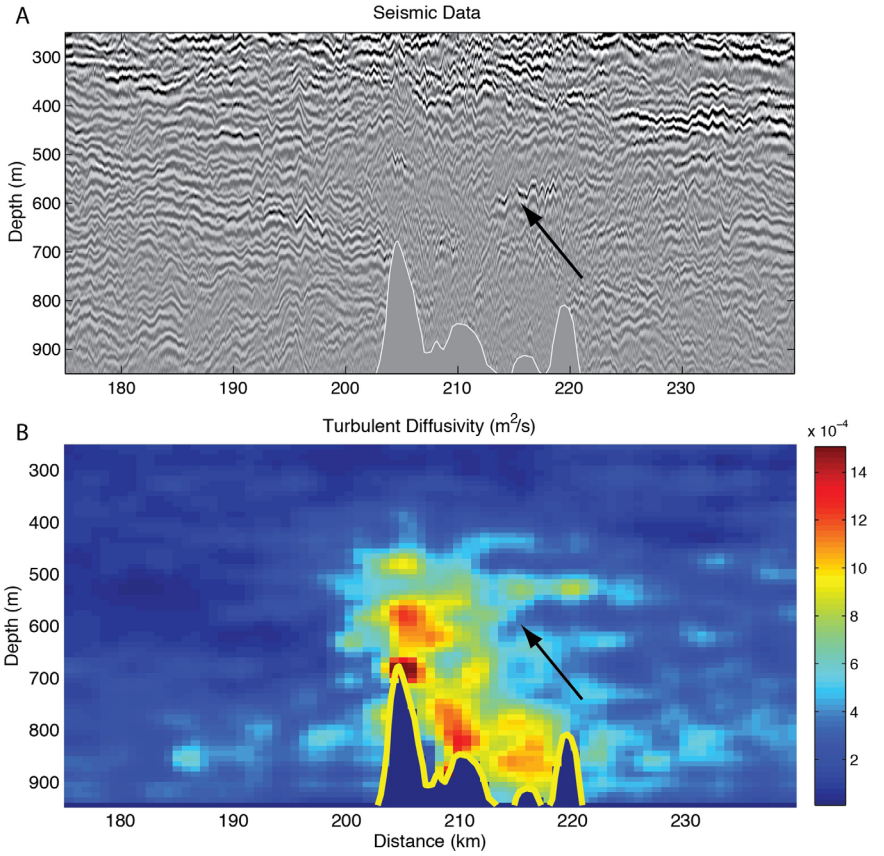

Figure 10. Above Heng-Chun ridge, line 4. (a) Seismic image showing reflections terminating at the peak of the ridge and lenses of seismically transparent water bounded by strong reflections such as that indicated by the black arrow. (b) Diffusivity above the ridge. Note the low diffusivity where seismic reflections are strong, indicated by the black arrow.

coherent reflections are weak, we observe elevated turbulent diffusivity. This result is expected; mixing waters would weaken thermohaline fine structure and reduce boundaries and gradients capable of reflecting seismic energy. Though imaging is weak, the combination of seismic amplitude spectra and traced displacement spectra can recover information contained in these weak zones [*Fortin et al*., 2016]. We note the similarity of our images to the model results of *Alford et al*. [2015] which show the breaking of an internal wave on a bathymetric high where turbulent zones are stretch around a layer of more stratified waters, identified by arrows in Figure 10. Estimates of turbulent diffusivity show the region above the ridge to be a stronger mixing hotspot than waters away from the ridge crest at similar depths with diffusivities ∼10 times greater than surrounding waters.

4.2. Line 5

Seismic line 5 crosses the Lan-Yu ridge from west-to-east and shows strong seismic reflections throughout (Figure 2b). Seismically transparent lenses are less common in line 5 than line 4 and mostly exist between 500 and 800 m. At the Lan-Yu ridge between 6 and 25 km, strong seismic reflections exist very close to the bathymetry and in some cases terminate at the seafloor. At the secondary ridge at 50 km, reflections are weaker due to attenuation of the source signal at depth and do not exhibit strong reflections coupled with seismically transparent zones indicative of internal wave breaking.

Spectral data from line 5 matches the characteristic slope of turbulence across horizontal wave numbers of 0.01–0.02 cpm (Figure 4). Tracked reflectors yield a diffusivity estimate of 9.3×10^{-5} m^2/s averaged across the entire transect. Internal wave spectra are recovered in the displacement spectra, but not the data transform (Figures 4b and 4d). Displacement spectra are displayed across wave numbers from 0.3× the lower turbulent boundary to 2× the upper turbulent boundary and recover characteristic internal wave energy by limiting the data to clear seismic reflections whereas data transforms include all data along an isobath. Over

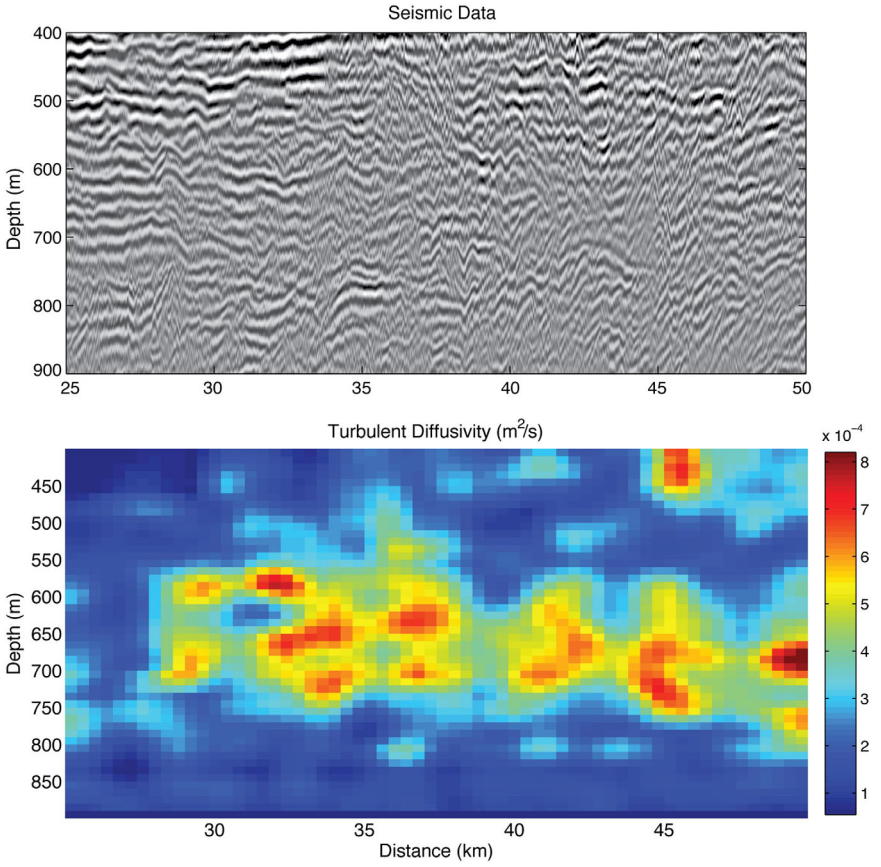

Figure 11. Highly turbulent midwater on line 5. (a) Seismic data and (b) turbulent diffusivities. Elevated diffusivity occurs where weaker, higher wave number seismic reflections are present.

long distances (here ~80 km) the data transforms break the isobath-isopycnal assumption necessary for slope spectra to mimic internal wave characteristics. Additionally, the data transform includes the muted section below the seafloor reducing the spectral energy at low wave numbers. Characteristic noise spectra are limited by band-pass filtering.

The turbulent diffusivity map of line 5 shows the highest levels of mixing to be in the midwater between seafloor highs between 500 and 800 m (Figure 7). Elevated turbulent diffusivity levels form an arcing band that is most shallow at the same depth as the top of the Lan-Yu ridge. Figure 11 highlights the strongest mixing in the band of elevated turbulence. The more seismically transparent regions in Figure 11 exhibit higher horizontal wave number reflections as well as increased turbulent diffusivity, an expected result. The bathymetric high and upper bound of the turbulent zone having the same depth likely indicates this patch of turbulence is a boundary between waters that can and cannot pass over the Lan-Yu ridge.

Figure 12 details the seismic reflections in the water column and associated turbulent diffusivities around the peak of the Lan-Yu ridge. Unlike line 4, the seismic reflections here exist very near the seabed and in some cases terminate upon the ridge slopes indicating a highly stratified water column. Elevated diffusivity exists on the east side of the ridge, in the same depth range as the midwater turbulence and in lenses of more seismically transparent water. Comparing this result to the model predictions of *Alford et al.* [2015], our observations resemble a time near or before an internal wave-breaking event on a seafloor high.

4.3. Line 9

Seismic line 9 crosses both the Heng-Chun and Lan-Yu ridges at the northern end of the Luzon Passage. Interaction between seismic reflections and bathymetry differs between the two ridges in this image (Figure

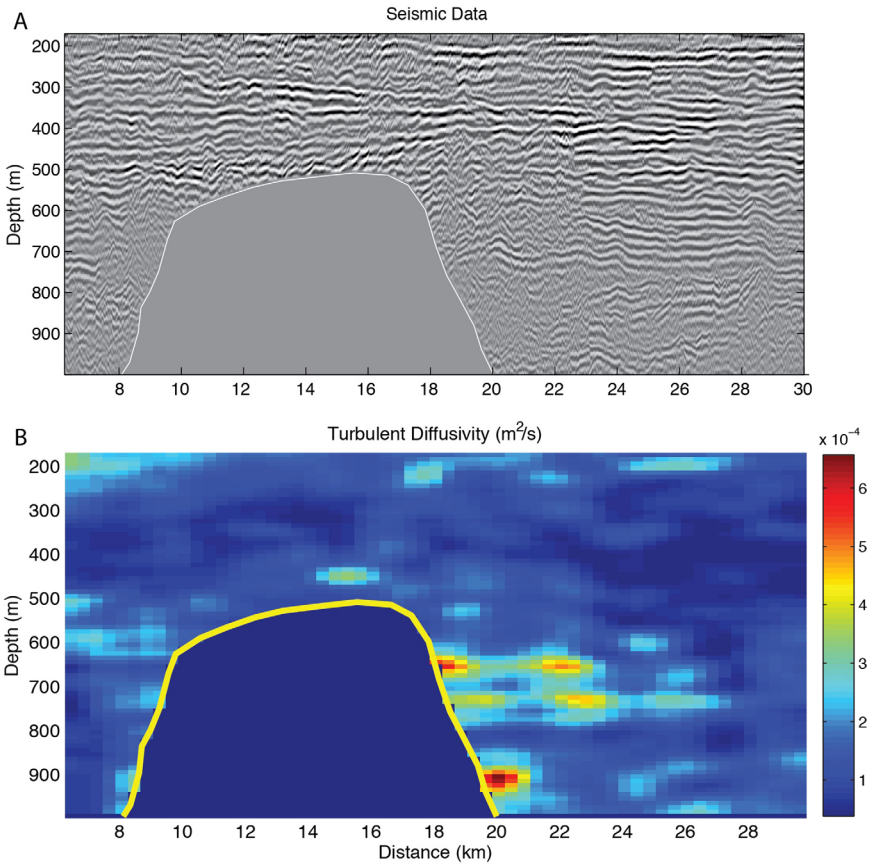

Figure 12. Above Lan-Yu ridge, line 5. (a) Seismic image showing strong reflections very near and terminating at the seafloor. (b) Diffusivity around the ridge. Note the low diffusivity throughout with the exception of the seismically transparent lenses.

2c). In the west at the Heng-Chun ridge, reflections exist near the seafloor and terminate along the slope in many places, similar to line 5. At the Lan-Yu ridge to the east, the ridge is surrounded by a combination of seismic reflections and seismically transparent zones, similar to those seen on line 4. The midwater has relatively consistent reflectivity throughout.

Spectral characteristics for both the data transform and displacement spectra show a turbulent subrange of 0.0075–0.0155 cpm (Figures 5b and 5d). Tracked reflectors yield an average diffusivity of 3.2×10^{-4} m^2/s over the entire transect. Displacement spectra are displayed across wave numbers from 0.3× the lower turbulent boundary to 2× the upper turbulent boundary. Characteristic internal wave spectra are present in the displacement spectra, but not the data transforms as in line 5. Noise is limited in the spectra by bandpass filtering.

Elevated turbulent diffusivity in line 9 is almost entirely limited to regions around the two ridges in deeper waters (Figure 8). However, the highest diffusivity is observed in a hotspot between the ridges similar in size (∼10 km by 150 m) and diffusivity ($\sim 5 \times 10^{-3}$ m^2/s) to those seen in line 4. Though similar in size and diffusivity to the elevated mixing seen in line 4, this hot spot is likely the result of a different generation mechanism. The adjacent waters below ∼1000 m in line 9 are similar in seismic character and we observe no internal wave pulses in the overlying water. It is possible this hotspot is the result of surface forcing from the Kuroshio current. Midwater regions away from the ridges are less turbulent and relatively homogeneous.

Comparing the two ridges in line 9, we see very different turbulent behaviors. At the Heng-Chun ridge to the west, there is little turbulence around the ridge top (Figure 13). Turbulence along the Heng-Chun ridge in deeper waters is consistently colocated with seismically transparent zones. The apparent lack of turbulence at local seafloor lows at ∼100 and ∼110 km are artifacts of the smoothing applied to the

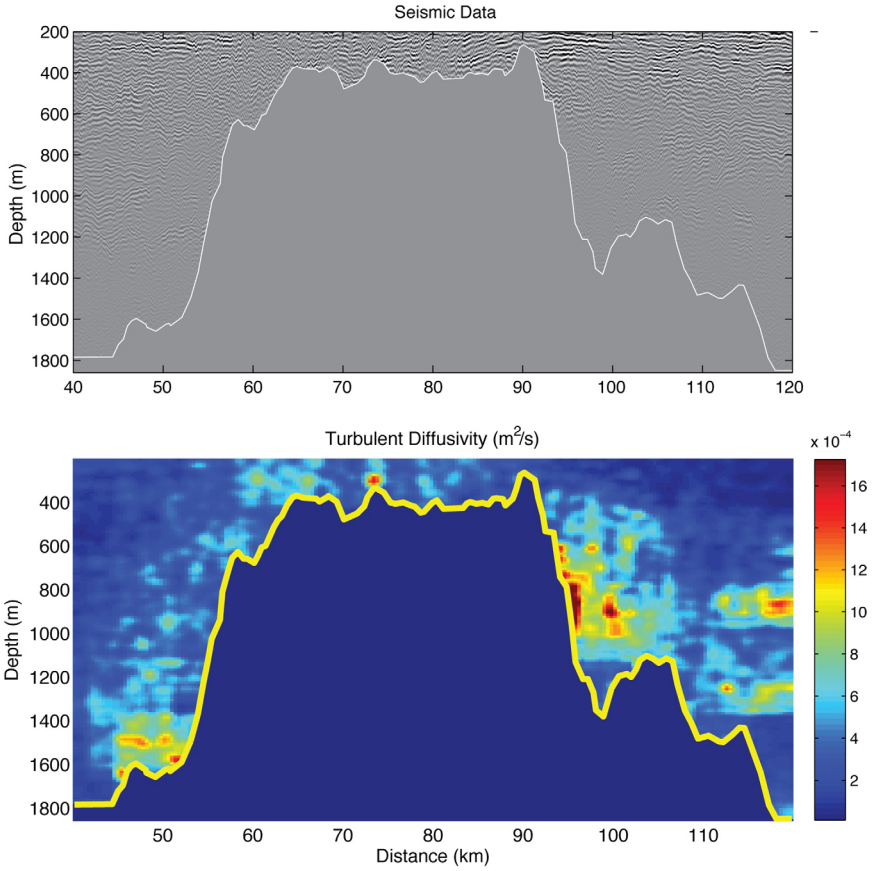

Figure 13. Heng-Chun ridge on line 9. (a) Seismic data and (b) turbulence where most diffusivity occurs in deeper waters at the slopes of the ridge. Little diffusivity above the ridge.

displacement spectra as a result of being surrounded by zero values below the seafloor; turbulent diffusivity in the local lows are likely the same or higher than the waters immediately above them. At the Lan-Yu ridge we see much more diffusivity above the ridge top (Figure 14). Additionally, there are pockets of elevated diffusivity bordered by strong seismic reflections, a result similar to that in line 4. These results suggest an internal wave is in the process of breaking at the Lan-Yu ridge in line 9, but not at the Heng-Chun ridge at the time of data collection.

4.4. Evidence for Geometric Resonance

The driving mechanism for the generation of nonlinear internal waves in the South China Sea is thought to be the interaction of tidal forces and bathymetric geometry which, over time, develop wave packets that take on a sinusoidal shape [*Alford et al*., 2010, 2015]. An alternate theory would attribute their generation to a hydraulic jump, such as in the Knight Inlet [*Farmer and Smith*, 1980] and the Strait of Gibralter [*Farmer and Armi*, 1988]. Both lee waves and sinusoidal internal waves between ridges would be expected if hydraulic jumps were the driving mechanism behind nonlinear internal wave generation in the South China Sea. However, in our data we observe no lee waves above bathymetric highs such as those seen in other seismic observations [*Eakin et al*., 2011; *Fortin et al*., 2016] or sinusoidal internal wave packets between ridges. While it is possible that the timing of data collection simply missed these features, we nonetheless do not observe such features. In contrast, we do observe a sinusoidal wave packet far west of the Heng-Chun and Lan-Yu ridges and evidence for a younger wave packet in line 4. Our image may capture two evolutionary stages of nonlinear wave evolution, or two wave types in a diurnal period as seen in *Alford et al*. [2010]. Our data suggest tidal forcing and the geometry of the bathymetry in the South China Sea largely drive the formation of nonlinear internal wave packets.

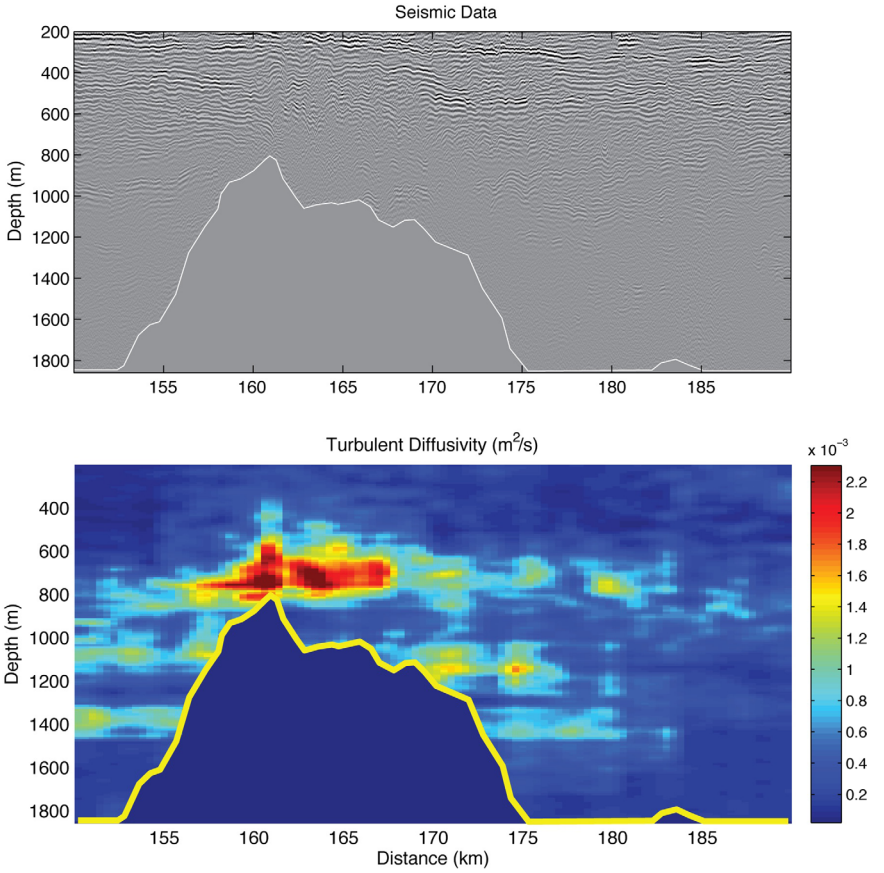

Figure 14. Lan-Yu ridge on line 9. (a) Seismic data and (b) turbulence where most diffusivity occurs above the ridge with similar strong reflections bounding turbulence zones.

5. Conclusions

We find elevated, heterogeneous mixing across the Heng-Chun and Lan-Yu ridges in the Luzon passage as evidenced by seismic data. Common to all three lines we present here, the highest levels of turbulence occur in deep and midwater regions. Elevated turbulence is also seen in lenses of water with low seismic reflectivity, usually sandwiched between bright reflections caused by strong thermal gradients, often found near bathymetric highs. At two ridge crests, we observe behavior similar to model predictions for breaking internal waves. We also observe a characteristic turbulence pattern associated with internal wave packets propagating away from the Heng-Chun and Lan-Yu ridges westward into the South China Sea. Overall, levels of turbulent diffusivity estimated from the seismic data span over two orders of magnitude from greater than 5×10^{-3} m^2/s to less than 5×10^{-5} m^2/s.

Our data support the argument that nonlinear internal wave pulses in the South China Sea are generated by interactions between tidal forces and seafloor geometry. We do not observe any large amplitude wave pulse disturbances to oceanic fine structure between the ridges, as we do west in the SCS interior. Additionally, we find no evidence for lee waves above the ridges in the seismic images or the turbulent diffusivity maps along any transect. The observation of a clear sinusoidal internal wave packet and another similar wave packet at the predicted location for one subsequent semidiurnal period suggests an evolution of internal wave packets radiating away from the Luzon Passage into the South China Sea.

Acknowledgments
The authors thank all members of the TAIGER research project, particularly D. Eakin for data collection as well as A. VonLanken and L. St. Laurent for helpful discussions. We also thank Chongzhi Dong and an anonymous reviewer of this paper for their help in improving the final manuscript. We thank the captain and crew of the *R/V Marcus Langseth*. Seismic data processing was done with Paradigm's *Echos* software and map figures were made using GeoMapApp. Seismic data can be found at the Academic Seismic Portal at UTIG (http://www-udc.ig.utexas.edu/sdc/). This work was funded by NSF grant 0648620 and ONR/DEPSCoR Grant DODONR40027.

References

Alford, M. H., R.-C. Lien, H. Simmons, J. Klymak, S. Ramp, Y. J. Yang, D. Tang, and M.-H. Chang (2010), Speed and evolution of nonlinear internal waves transiting the South China Sea, *J. Phys. Oceanogr.*, *40*(6), 1338–1355, doi:10.1175/2010jpo4388.1.

Alford, M. H., et al. (2015), The formation and fate of internal waves in the South China Sea, *Nature*, *521*(7550), 65–69, doi:10.1038/nature14399.

Bornstein, G., B. Biescas, V. Sallarès, and J. F. Mojica (2013), Direct temperature and salinity acoustic full waveform inversion, *Geophys. Res. Lett.*, *40*, 4344–4348, doi:10.1002/grl.50844.
Buijsman, M. C., J. M. Klymak, S. Legg, M. H. Alford, D. Farmer, J. A. MacKinnon, J. D. Nash, J. Park, A. Pickering, and H. Simmons (2014), Three-dimensonal double-ridge internal tide resonance in Luzon Strait, *J. Phys. Oceanogr.*, *44*, 850–869, doi:10.1175/JPO-D-12-024.1.
Eakin, D., W. S. Holbrook, and I. Fer (2011), Seismic reflection imaging of large-amplitude lee waves in the caribbean sea, *Geophys. Res. Lett.*, *38*, L21601, doi:10.1029/2011GL049157.
Farmer, D. M., and L. Armi (1988), The flow of atlantic water through the strait of gibralter—The flow of the mediterranean water through the strait of gibralter, *Prog. Oceanogr.*, *21*(1), 1–105, doi:10.1016/0079-6611(88)90055-9.
Farmer, D. M., and J. D. Smith (1980), Tidal interaction of stratified flow with a sill in knight inlet, *Deep Sea Res., Part A*, *27*(3–4), 239–254, doi:10.1016/0198-0149(80)90015-1.
Fortin, W. F. J., and W. S. Holbrook (2009), Sound speed requirements for optimal imaging of seismic oceanography data, *Geophys. Res. Lett.*, *36*, L00D01, doi:10.1029/2009GL038991.
Fortin, W. F. J., W. S. Holbrook, and R. W. Schmitt (2016), Mapping turbulent diffusivity associated with oceanic internal lee waves offshore Costa Rica, *Ocean Sci.*, *12*, 601–612, doi:10.5194/os-12-601-2016.
Garrett, C. (2003), Internal tides and ocean mixing, *Science*, *301*(5641), 1858–1859.
Garrett, C., and W. Munk (1975), Space-time scales of internal waves: A progress report, *J. Geophys. Res.*, *80*(3), 291–297, doi:10.1029/JC080i003p00291.
Gregg, M. C. (2002), Flow, water mass changes, and hydraulics in the bosphorus, *J. Geophys. Res.*, *107*(C3), 3016, doi:10.1029/2000JC000485.
Holbrook, W. S., and I. Fer (2005), Ocean internal wave spectra inferred from seismic reflection transects, *Geophys. Res. Lett.*, *32*, L15604, doi:10.1029/2005GL023733.
Holbrook, W. S., P. Paramo, S. Pearse, and R. W. Schmitt (2003), Thermohaline fine structure in an oceanographic front from seismic reflection profiling, *Science*, *301*(5634), 821–824.
Holbrook, W. S., I. Fer, R. W. Schmitt, D. Lizarralde, J. M. Klymak, L. C. Helfrich, and R. Kubichek (2013), Estimating oceanic turbulence dissipation from seismic images, *J. Atmos. Oceanic Technol.*, *30*(8), 1767–1788, doi:10.1175/jtech-d-12-00140.1.
Huang, X., H. Song, Y. Bai, J. Chen, and B. Liu (2012), Estimation of seawater movement based on reflectors from a seismic profile, *Acta Oceanol. Sin.*, *31*(5), 46–53, doi:10.1007/s13131-012-0235-7.
Jackson, C. (2007), Internal wave detection using the moderate resolution imaging spectroradiometer (modis), *J. Geophys. Res.*, *112*, C11012, doi:10.1029/2007JC004220.
Jackson, C. R. (2009), An empirical model for estimating the geographic location of nonlinear internal solitary waves, *J. Atmos. Oceanic Technol.*, *26*(10), 2243–2255, doi:10.1175/2009JTECHO638.1.
Jan, S., R.-C. Lien, and C.-H. Ting (2008), Numerical study of baroclinic tides in luzon strait, *J. Oceanogr.*, *64*(5), 789–802, doi:10.1007/s10872-008-0066-5.
Klaeschen, D., R. W. Hobbs, G. Krahmann, C. Papenberg, and E. Vsemirnova (2009), Estimating movement of reflectors in the water column using seismic oceanography, *Geophys. Res. Lett.*, *36*, L00D03, doi:10.1029/2009GL038973.
Klymak, J. M., and M. C. Gregg (2004), Tidally generated turbulence over the knight inlet sill, *J. Phys. Oceanogr.*, *34*(5), 1135–1151, doi:10.1175/1520-0485(2004)034 < 1135:TGTOTK>2.0.CO;2.
Klymak, J. M., and J. N. Moum (2007a), Oceanic isopycnal slope spectra. Part i: Internal waves, *J. Phys. Oceanogr.*, *37*(5), 1215–1231, doi:10.1175/jpo3073.1.
Klymak, J. M., and J. N. Moum (2007b), Oceanic isopycnal slope spectra. Part ii: Turbulence, *J. Phys. Oceanogr.*, *37*(5), 1232–1245, doi:10.1175/jpo3074.1.
Klymak, J. M., R. Pinkel, C. Liu, A. K. Liu, and L. David (2006), Prototypical solitons in the South China Sea, *Geophys. Res. Lett.*, *33*, L11607, doi:10.1029/2006GL025932.
Krahmann, G., P. Brandt, D. Klaeschen, and T. Reston (2008), Mid-depth internal wave energy off the iberian peninsula estimated from seismic reflection data, *J. Geophys. Res.*, *113*, C12016, doi:10.1029/2007JC004678.
McIntosh, K., L. Lavier, H. van Avendonk, R. Lester, D. Eakin, and C.-S. Liu (2014), Crustal structure and inferred rifting processes in the northeast South China Sea, *Mar. Petrol. Geol.*, *58*, 612–626, doi:10.1016/j.marpetgeo.2014.03.012.
Nandi, P., W. S. Holbrook, S. Pearse, P. Paramo, and R. W. Schmitt (2004), Seismic reflection imaging of water mass boundaries in the norwegian sea, *Geophys. Res. Lett.*, *31*, L23311, doi:10.1029/2004GL021325.
Niwa, Y., and T. Hibiya (2001), Numerical study of the spatial distribution of the m-2 internal tide in the pacific ocean, *J. Geophys. Res.*, *106*(C10), 22,441–22,449, doi:10.1029/2000JC000770.
Osborn, T. R. (1980), Estimates of the local-rate of vertical diffusion from dissipation measurements, *J. Phys. Oceanogr.*, *10*(1), 83–89, doi:10.1175/1520-0485(1980)010 < 0083:EOTLRO>2.0.CO;2.
Osborn, T. R., and C. S. Cox (1972), Oceanic fine structure, *Geophys. Fluid Dyn.*, *3*(1), 321–345, doi:10.1080/03091927208236085.
Papenberg, C., D. Klaeschen, G. Krahmann, and R. W. Hobbs (2010), Ocean temperature and salinity inverted from combined hydrographic and seismic data, *Geophys. Res. Lett.*, *37*, L04601, doi:10.1029/2009GL042115.
Ramp, S. R., T. Y. Tang, T. F. Duda, J. F. Lynch, A. K. Liu, C. S. Chiu, F. L. Bahr, H. R. Kim, and Y. J. Yang (2004), Internal solitons in the northeastern South China Sea—Part i: Sources and deep water propagation, *IEEE J. Oceanic Eng.*, *29*(4), 1157–1181, doi:10.1109/Joe.840839.
Rudnick, D. L., et al. (2003), From tides to mixing along the hawaiian ridge, *Science*, *301*(5631), 355–357, doi:10.1126/science.1085837.
Sallarès, V., B. Biescas, G. Buffett, R. Carbonell, J. J. Dañobeitia, and J. L. Pelegrí (2009), Relative contribution of temperature and salinity to ocean acoustic reflectivity, *Geophys. Res. Lett.*, *36*, L00D06, doi:10.1029/2009GL040187.
Sheen, K. L., N. J. White, and R. W. Hobbs (2009), Estimating mixing rates from seismic images of oceanic structure, *Geophys. Res. Lett.*, *36*, L00D04, doi:10.1029/2009GL040106.
Sheen, K. L., N. J. White, C. P. Caulfield, and R. W. Hobbs (2011), Estimating geostrophic shear from seismic images of oceanic structure, *J. Atmos. Oceanic Technol.*, *28*(9), 1149–1154, doi:10.1175/jtech-d-10-05012.1.
Simmons, H. L., R. W. Hallberg, and B. K. Arbic (2004), Internal wave generation in a global baroclinic tide model, *Deep Sea Res., Part I*, *51*(25–26), 3043–3068, doi:10.1016/j.dsr2.2004.09.015.
Sreenivasan, K. R. (1996), The passive scalar spectrum and the obukhov-corrsin constant, *Phys. Fluids*, *8*(1), 189–196, doi:10.1063/1.868826.
St. Laurent, L. C., J. M. Toole, and R. W. Schmitt (2001), Buoyancy forcing by turbulence above rough topography in the abyssal brazil basin, *J. Phys. Oceanogr.*, *31*(12), 3476–3495, doi:10.1175/1520-0485(2001)031 < 3476:BFBTAR>2.0.CO;2.
Thorpe, S. A. (2005), *The Turbulent Ocean*, Cambridge Univ. Press, New York.
Tian, J., Q. Yang, and W. Zhao (2009), Enhanced diapycnal mixing in the South China Sea, *J. Phys. Oceanogr.*, *39*(12), 3191–3203, doi:10.1175/2009jpo3899.1.

Von Lanken, A. (2012), Seismic oceanography investigation of nonlinear internal waves in the South China Sea, dissertations and theses, University of Wyoming, Laramie, Wyo.

Wesson, J. C., and M. C. Gregg (1994), Mixing at camarinal sill in the strait of gibraltar, *J. Geophys. Res.*, *99*(C5), 9847–9878, doi:10.1029/94JC00256.

Wood, W. T., W. S. Holbrook, M. K. Sen, and P. L. Stoffa (2008), Full waveform inversion of reflection seismic data for ocean temperature profiles, *Geophys. Res. Lett.*, *35*, L04608, doi:10.1029/2007GL032359.

Wu, F. T., H. Kuo-Chen, and K. D. McIntosh (2014), Subsurface imaging, taiger experiments and tectonic models of taiwan, *J. Asian Earth Sci.*, *90*, 173–208, doi:10.1016/j.jseaes.2014.03.024.

Yilmaz, O. (1987), *Seismic Data Processing*, 526 pp., Soc. of Explor. Geophys., Tulsa, Okla.

Zhao, Z. X., V. Klemas, Q. N. Zheng, and X. H. Yan (2004), Remote sensing evidence for baroclinic tide origin of internal solitary waves in the northeastern South China Sea, *Geophys. Res. Lett.*, *31*, L06302, doi:10.1029/2003GL019077.